Research Article | Vol. 33, No. 12 / 16 Jun 2025 / Optics Express 24249

Optics EXPRESS

Spatial coherence measurement and control in multimode fibers

JIAQI LI, PIOTR RYCZKOWSKI, AND GOËRY GENTY

Photonics Laboratory, Physics Unit, Tampere University, 33014 Tampere, Finland

Abstract: Light sources based on multimode fibers allow for controlling the degree of spatial coherence, which can be crucial for applications in sensing and imaging. Understanding the underlying mechanisms of coherence reduction and control in multimode fibers is then essential for optimized performance in these applications. In this study, we perform spatial coherence measurements across the full beam of multimode fiber based light sources using a wavefront-folding interferometer. By generating interferograms at different optical path difference positions from the fiber far-field output, the degree of spatial coherence can be quantified across the entire beam from the fringes' visibility. An approach for quantitative control of coherence is also developed providing insights for applications requiring tailored coherence properties. Our experimental results are further confirmed by numerical simulations using a linearly polarized eigenmode expansion and random modal coupling model.

1. Introduction

In recent years, there has been a growing interest for spatially incoherent or partially incoherent light sources in various scientific and commercial applications, including, e.g., laser speckle contrast imaging [1,2], spectral imaging [3,4], and space-free optical communication [5]. The speckle-like pattern resulting from the mutual interference of different spatial wavefronts directly relates to the degree of spatial coherence and significantly impacts the performance of spatial imaging and sensing, since it determines the achievable spatial resolution [1]. Several methods have been developed to control the spatial coherence of light sources, including temporal averaging techniques based on ground-glass rotation [6], wavelength diversity [7], or the combination of temporal, spatial, and angular diversity [8]. Coherence control can also be effectively achieved by guiding light through a multimode optical fiber (MMF) [2,8,9] and understanding the underlying physics of coherence control in MMFs is important for practical applications and further developments.

Early theoretical studies focused on extending the Van-Citter Zernike theorem from free-space to fibers by restricting the numerical aperture and obtaining fully incoherent modes [10]. Subsequent studies also analyzed the influence of the source bandwidth and fiber length on the spatial coherence at the MMF output [11,12]. Realistic distribution of mode amplitudes influenced by the injection conditions was further considered and shown to have a significant impact on the spatial coherence distribution in MMF [13]. Experimental studies have explored the effect of source bandwidth [14], fiber length and core size [15], and highlighted the strong influence of the relative modal amplitudes on the MMF output spatial coherence [16].

The quantitative characterization of spatial coherence typically relies on measuring the two-point correlation function of the optical field across its spatial distribution [17], but this measurement alone does not provide the true degree of spatial coherence without normalizing the interfering fields. Young's two-pinhole interference is an effective method to measure the coherence of light sources [18] but characterizing the spatial coherence across a full beam requires a raster scan which is very tedious. Wavefront-folding interferometry (WFI) on the other

#558061 https://doi.org/10.1364/OE.558061
Journal © 2025 Received 5 Feb 2025; revised 27 Mar 2025; accepted 15 Apr 2025; published 2 Jun 2025

hand has gained attention as a promising technique for coherence characterization [19–21] due to its high efficiency, parallel propagation, and capability to measure arbitrary fields that do not necessarily follow the Schell model [21]. In MMFs, the speckle contrast has been generally considered as an indicator of the spatial coherence and it is extensively used in speckle-contrast imaging [2]. However, it is important to emphasize that a reduced speckle contrast does not necessarily correspond to a decrease in spatial coherence [14].

Here, we study the spatial coherence across the full beam of multimode fiber light sources using WFI. The degree of spatial coherence is characterized across the beam from the fringes' visibility of the spatially-resolved interferograms recorded as a function of optical path difference. We show that the spatial coherence of a broadband source is significantly reduced due to the fact that the spatial phase of the different spectral components is randomized spatially by the MMF. We also develop an approach for quantitative control of coherence based on the spectrally-dependent speckle pattern at the MMF output. Our experimental observations are confirmed by numerical simulations using a linearly polarized eigenmode expansion and random modal coupling model.

2. Experimental measurements

Our experimental setup is shown in Fig. 1. The beam from the MMF output is collimated and sent to a WFI. A half waveplate/polarizer combination is used to control the intensity. In the first arm (A1), the beam is flipped with respect to the vertical direction compared to the beam. The total field then corresponds to the overlap of the original field with its mirror replica. Only on the central line of pixels of the camera the field overlaps with itself, and the resulting interference pattern is measured as a function of optical path difference between the two arms. The coherence degree between two points (for example P1, P2 in Fig. 1) at distance y along the vertical axis and separated by a distance Δx in the horizontal direction can be obtained from the interference fringes visibility measured at each camera pixel and normalized by the intensity distribution of the two arms [21]:

$$\gamma(\Delta x, y) = V(\Delta x, y)\left[\frac{2\sqrt{I\left(\frac{\Delta x}{2}, y\right)\Delta I\left(-\frac{\Delta x}{2}, y\right)}}{I\left(\frac{\Delta x}{2}, y\right) + I\left(-\frac{\Delta x}{2}, y\right)}\right]^{-1} \tag{1}$$

where V represents the fringes visibility. $I\left(\frac{\Delta x}{2}, y\right)$ and $I\left(-\frac{\Delta x}{2}, y\right)$ represent the spatial intensity at positions $\frac{\Delta x}{2}$ and $-\frac{\Delta x}{2}$, respectively and they are obtained by blocking separately each arm of the interferometer.

We emphasize that, here, in contrast with the approach presented in Ref. 10 where the measurements are performed at two fixed positions in the transverse plane, the degree of spatial coherence across the full 2D plane is measured. We characterized the spatial coherence at the MMF fiber output using two different types of light sources: an amplified spontaneous emission (ASE) and a wavelength-tunable quasi-monochromatic laser. The step-index MMF with a 0.22 numerical aperture (NA) is 11 m long with a core diameter of 105 µm. The ASE source is generated from a 1-m erbium-doped fiber and its spectrum is shown in the inset of Fig. 1 with a -20 dB bandwidth exceeding 45 nm. The spatial intensity distribution observed at the MMF output is near-Gaussian as shown in Fig. 2(a) and the corresponding spatial coherence extracted from the spatially-resolved interferograms is plotted in Fig. 2(b). For completeness, an example of interferogram recorded from a single camera pixel as a function of optical path difference between the two arms is shown in Fig. 2(c).

Although the spatial intensity distribution looks near-Gaussian, one can see that the coherence degree (outside the central overlapping area) is in fact very low across the entire beam, with

Optics EXPRESS

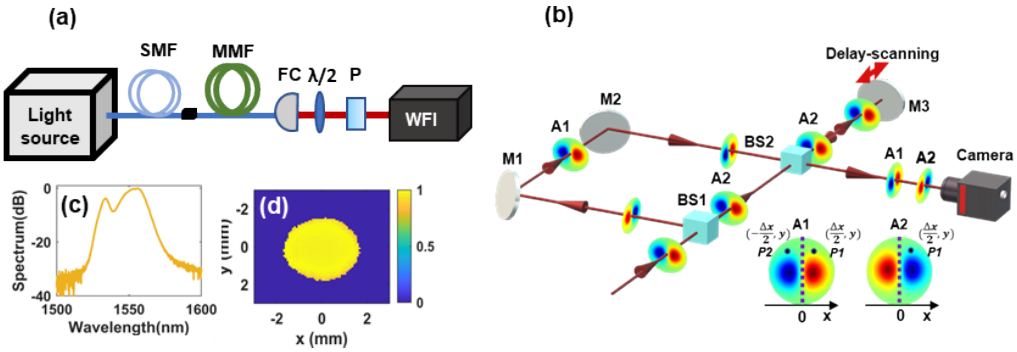

Fig. 1. Experimental setup for spatial coherence measurement based on WFI. (a) shows the overall setup, SMF: single mode fiber, FC: fiber collimator, λ/2: half waveplate, P: polarizer. (b) illustrates the WFI and how it produces an interference between the MMF fiber output beam and its mirror replica allowing for characterizing the spatial coherence. M: mirror, BS: beam splitter. M3 is mounted on a piezo-electric stage for optical path difference-scanning between the two arms. (c) and (d) show the spectrum and measured spatial coherence of the ASE source.

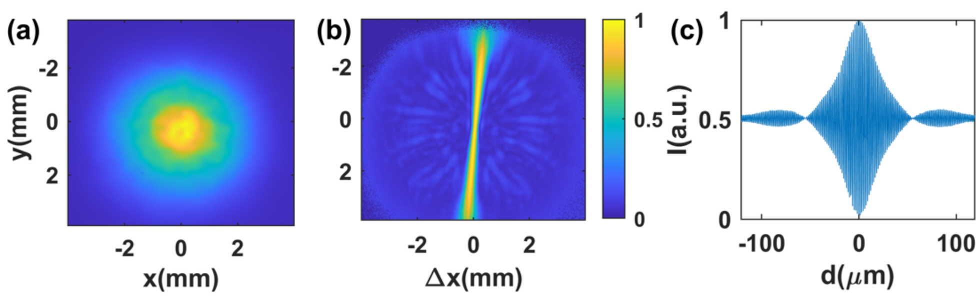

Fig. 2. Spatial coherence of the ASE source. (a) Spatial intensity distribution at the MMF output, (b) degree of spatial coherence $\gamma(\Delta x, y)$, (c) single-pixel interferogram recorded as a function of optical path difference d.

an average value less than 0.3, indicating that the beam at the output of the multimode fiber is spatially incoherent. This incoherence arises from the large spectral bandwidth of the light source that leads to phase scrambling combining the modal dispersion in the MMF.

In order to highlight the key role of the spectral bandwidth in the decoherence process, we conducted spatial coherence measurement of a quasi-monochromatic tunable CW laser with 10 kHz linewidth (Topica CTL1500) after propagation in the same MMF. The results are shown in Fig. 3 where one can see that the spatial intensity distribution is not uniform and that the beam is highly speckled as the result of interference between multiple modes. Note that the beam at the fiber output was expanded to ensure that the size of the camera pixels is smaller than the speckle size and therefore that only the central part of the beam that fits in the camera detection area (about half of the size) was characterized. In the regions of low intensity of the speckled beam, interference fringes vanish due to the camera detection noise and the degree of spatial coherence cannot be evaluated in those spatial locations. This means that a spatial filter to mask the area of low intensity needs to be applied before extracting the coherence degree (see Fig. 3(c)). The degree of spatial coherence is illustrated in Fig. 3(d) with values exceeding 0.85 across the characterized area. For a quasi-monochromatic light source, the phase difference between arbitrary points in the transverse plane is maintained, resulting in high spatial coherence.

This phase difference is however wavelength-dependent such that if the wavelength of the light source is tuned, the speckle pattern will change. This is shown in Fig. 4, where we plot the spatial intensity recorded at the MMF output when the wavelength of the CW laser is tuned in steps of 0.1 nm. This explains the low coherence observed for a broadband source where the wavelength-dependent propagation constants lead to different and randomized phase distributions for various wavelengths, effectively reducing the spatial coherence.

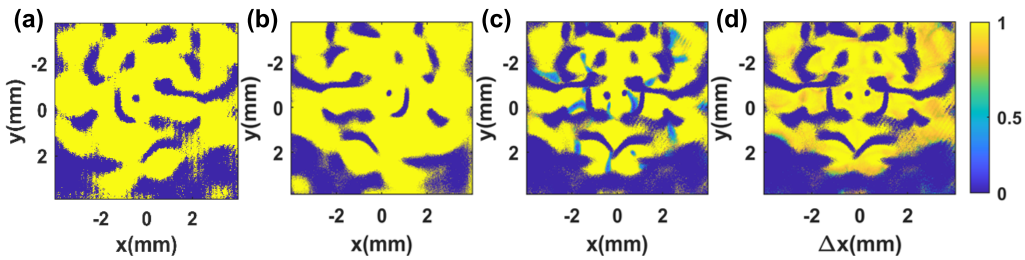

Fig. 3. Spatial coherence at the MMF output of the quasi-monochromatic laser. (a) and (b) Measured speckle patterns from the two arms. (c) Filter applied to mask the area where light intensity is near-zero (see text for more details). (d) Degree of spatial coherence.

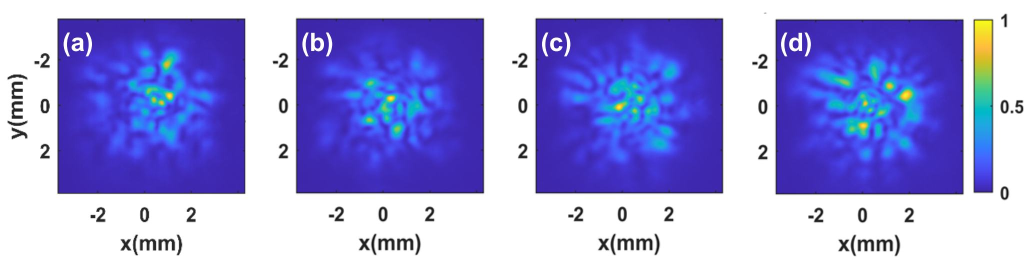

Fig. 4. Spatial intensity profile measured at the output of the MMF for a quasi-monochromatic source with wavelength at (a) 1550 nm, (b) 1550.1 nm, (c) 1550.2 nm, and (d) 1550.3 nm.

3. Numerical simulations

In order to simulate the spatial coherence at the output of the MMF, we use an eigenmode expansion from the incident field onto the linearly polarized modes basis of the fiber. Energy exchange between the different modes is included using random coupling modelled by a Gaussian distribution calibrated from the experimentally measured speckle contrast at the fiber output. We describe below in more details the different steps of the model.

3.1. Linearly polarized modes

Conventional MMFs are weakly guiding, and the electric field can be represented as a combination of linearly polarized (LP) modes. In step-index fibers with radially symmetric refractive index profile, the transverse amplitude distribution Ψ of LP modes can be written as [22]:

$$\Psi(u) = R(r)\Theta(\varphi) \tag{2}$$

Optics EXPRESS

where R and Θ are functions that only depends on the radial coordinate r and azimuthal angle φ, respectively:

$$R(r) = C \cdot \begin{cases} \frac{J_l(Ur/a)}{J_l(U)}, & r<a \\ \frac{K_l(Wr/a)}{K_l(W)}, & r \geq a \end{cases} \quad \text{and} \quad \Theta(\varphi) = \begin{cases} \cos(l\varphi) \\ \sin(l\varphi) \end{cases} \tag{3}$$

Here, C is a constant, a denotes the core radius, and J_l and K_l represent the Bessel function of the first kind and modified Bessel function of second kind of order l, respectively. U and W are the normalized transverse phase and attenuation constants, respectively, and they are determined by the eigenvalue equation:

$$U\frac{J_{n+1}(U)}{J_n(U)} = K\frac{K_{n+1}(W)}{K(W)}; U^2 + W^2 = V^2 \tag{4}$$

$$U = a\sqrt{k_0^2 n_{core}^2 - \beta^2}; W = a\sqrt{\beta^2 - k_0^2 n_{clad}^2} \tag{5}$$

where β is the propagation constant of the mode and $V = ak_0\sqrt{n_{core}^2 - n_{clad}^2} = ak_0 NA$ (NA is the numerical aperture of fiber) governs the number of guided modes.

3.2. Eigenmode expansion

From the eigenvalue equation, one can compute the LP modes supported by a specific step-index fiber. Previous theoretical studies have typically analyzed the mechanism of decoherence in MMFs by assigning random values or particular statistical distributions to the mode amplitude [10]. However, the modes amplitude distribution is significantly influenced by the injection conditions, which in turn can strongly influence the spatial coherence at the fiber output. It is therefore important to account for the injection condition to evaluate the relative mode amplitude distribution at the fiber output. In this context, we employ an eigenmode expansion method (EEM) [23] to calculate the modes amplitude at the fiber input from any arbitrary incident field. To maintain consistency with the experiments reported below, a 2D Gaussian field is employed to model the incident field:

$$\Psi_{in}(\bar{x}, \bar{y}) = A_0 e^{-\frac{\bar{x}^2+\bar{y}^2}{w_0{}^2}} e^{-ik_0 q sin\theta}, q \in \{x, y\} \tag{6}$$

where w_0 denotes the radius at which the field amplitude decreases to 1/e of its maximum value. The coordinates x and y represent the transverse coordinates of the fiber, with the origin taken at the center of the fiber core. The incident location on the fiber transverse plane is denoted as (x_0, y_0), and the relative coordinates are defined as $\bar{x} = x - x_0$, $\bar{y} = y - y_0$. The parameter θ represents the incident angle with respect to the x- and y-axis. $k_0 = 2\pi/\lambda$ is the wavenumber in free space. We redefine the order of LP modes as m, determined by the effective refractive index, and the intensity of each eigenmode mode φ_m is normalized to unity:

$$\iint |\varphi_m(x, y)|^2 dxdy = 1 \tag{7}$$

with the eigenmodes orthogonal to each other

$$\iint \varphi_m(x, y)\varphi_n{}^*(x, y)dxdy = 0, m \neq n. \tag{8}$$

Any arbitrary field incident onto the fiber entrance facet can then be decomposed into LP modes [23]:

$$\Psi_{in}(\bar{x}, \bar{y}) = \sum\nolimits_m^M c_{m0}\varphi_m(x, y), \ \sum\nolimits_m^M c_{m0}{}^2 = 1 \tag{9}$$

and the relative amplitude of each mode at the fiber input can be obtained from:

$$c_{m0} = \iint \Psi_{in}(\bar{x}, \bar{y})\varphi_m{}^*(x, y)dxdy. \tag{10}$$

3.3. Mode coupling

In an ideal scenario, the modes excited by a specific injected field should propagate unperturbed in a step-index MMF. However, in the case of a long propagation distance, energy exchange between the different modes becomes significant, primarily due to accumulated perturbations in the refractive index caused e.g. by fiber inhomogeneities and environmental disturbances such as bending, vibrations, or temperature fluctuations. Consequently, the modes amplitude distribution does not remain constant during propagation. Accounting both for the modal dispersion and the propagation dependent modes amplitude, the field after propagation over a distance z in the MMF can be expressed as:

$$\Psi(z) = \sum_m^M c_m(z)\varphi_m e^{i\beta_m z} \tag{11}$$

where β_m represents the propagation constant of mode m and $c_m(z)$ is the propagation-dependent amplitude of mode m. The determination of $c_m(z)$ depends both on the initial coefficient $c_{m0} = c_m(z=0)$ and the perturbations in the refractive index along the fiber. Calculating $c_m(z)$ becomes exceedingly intricate and challenging due to numerous factors influencing the refractive index. An alternative phenomenological approach was introduced in [13] where coupling between neighboring modes with similar effective propagation constants generally dominates, while coupling with other modes is at least an order of magnitude weaker [24]. Mode coupling can then be described by multiplying the initial amplitude of mode m by a Gaussian distribution function $G_m = \exp\left[-\frac{(x-\mu_m)^2}{2\sigma^2}\right]$ where $x = (\beta_0,\ \beta_1, \ldots, \beta_M)/\beta_M$ is the normalized modal propagation constant. The parameter $\mu_m = \frac{\beta_m}{\beta_M}$ represents the effective propagation constant normalized by the maximum modal propagation constant β_M. The parameter σ determines the strength of the mode coupling, which can be calibrated from the measured speckle pattern at distance z. Note that upon this transformation the total power is conserved and $\sum_m^M {c_m}^2 = 1$ is satisfied.

3.4. Spatial coherence simulations

The LP modes are computed as described in sections 3.1 and 3.2 using the parameters of the fiber from our experiments. Specifically, the refractive indices of the fiber core and cladding are 1.465 and 1.444, respectively, and the numerical aperture is 0.247. The fiber supports more than 400 modes at 1550 nm. The modal amplitudes at the fiber input determined from Eqs. (9–10) are shown in Fig. 5(a). Note that, here, factors such as incident angle and incident position deviation are taken to be 0 since the light source is directly connected to the MMF from a SMF. This also leads to the preferential excitation of LP_0 k modes (k integer) and a discrete modal amplitude distribution as seen in Fig. 5(a). Energy exchange between different modes due to local perturbations in the refractive index is calculated as described in section 3.3 using a 1D Gaussian distribution with a coupling strength σ=0.02 calibrated from the speckle contrast in our experiments. The resulting modal amplitudes at the fiber output are shown in Fig. 5(b) where one can see that mode coupling leads to the energy being leaked to a large number of higher-order non-LP_0 k modes and yielding a continuous energy redistribution among the modes.

We further assume that we are in the stationary regime where the fiber length is much longer than the coupling length between the different modes [13]. With this assumption, the field amplitude at a particular wavelength at the fiber output can be evaluated from Eq. (11). The modal dispersion of the MMF results in spatially randomized phases across the transverse plane, leading to a speckle-like interference pattern. This is illustrated in Fig. 6 which shows the far-field spatial intensity associated with different wavelengths in step of 0.1 nm similar to those recorded experimentally and shown in Fig. 4. The modal amplitude distribution was adjusted to get the same speckle contrast as in the experiments above with the quasi-monochromatic source.

We next mimic the experimental spatial coherence measurements in our simulations. More specifically, by applying Fourier transform on the simulated field Ψ_λ at the fiber output for a

Optics EXPRESS

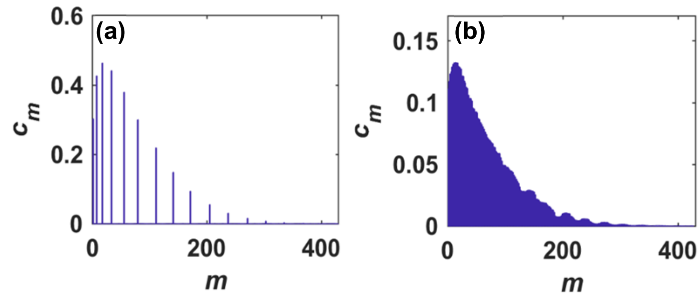

Fig. 5. Simulated modal amplitudes at (a) MMF input and (b) MMF output.

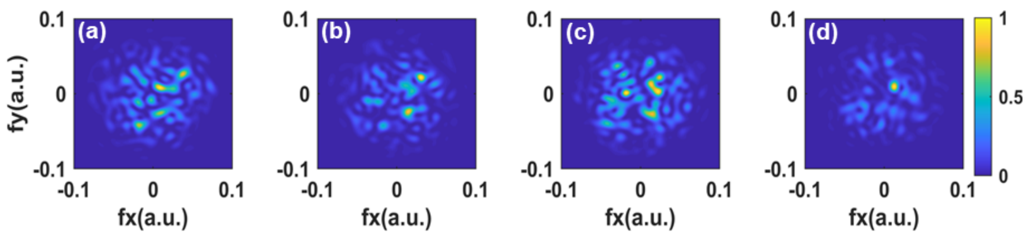

Fig. 6. Simulated far-field spatial intensity at the MMF output for quasi-monochromatic source with wavelength at (a) 1550.0 nm, (b) 1550.1 nm, (c) 1550.2 nm, and (d) 1550.3 nm. fx and fy denotes the spatial frequencies in Fourier domain.

given spectral component at wavelength λ, one can obtain the far-field distribution $\mathcal{F}\{\Psi_\lambda\}$ and its mirrored replica $\mathcal{F}\{\Psi^f_\lambda\}$ where $\mathcal{F}$ denotes Fourier transform. The resulting interferogram as a function of optical path d difference between the two beams can be represented as $\left|\sum_\lambda(\mathcal{F}\{\Psi_\lambda\}\cdot e^{ik_\lambda d}+\mathcal{F}\{\Psi^f_\lambda\})\right|^2=\sum_\lambda|\mathcal{F}\{\Psi_\lambda\}\cdot e^{ik_\lambda d}+\mathcal{F}\{\Psi^f_\lambda\}|^2$ considering that the exposure time in our experiment is about 1 ms. The maximum and minimum intensity of the interferogram are obtained at each spatial position by varying the optical path difference and the degree of spatial coherence is computed in the far field from the fringes visibility as was done in the experimental data processing. Figure 7 shows the simulated spatial coherence at the MMF output both for a monochromatic laser source and a broadband incoherent field constructed from 25 independent monochromatic spectral components with a 0.2 nm wavelength-spacing. One can see that the simulated degree of coherence agrees well with our experimental observations: the beam is spatially fully coherent for a monochromatic laser source (note that the numerical model does not include any detection noise such that the spatial coherence can be calculated at every spatial location of the beam) while for a broadband spectrally incoherent light similar to the ASE source there is only a narrow band with a high degree of coherence corresponding to the camera central pixels where the field overlaps with itself.

While propagation in a MMF is in principle deterministic, one can explain the decoherence process from the input characteristics of the light source. When a broadband spatially coherence source such as the single-mode fiber-based ASE source used here is injected into a MMF, light is coupled into a large number of modes depending on the injection conditions and mode coupling within the fiber arising from local perturbations. Initially, the phases of the excited modes remain correlated over a short propagation distance such that the field maintains a certain degree of spatial coherence. However, due to modal dispersion, different modes propagate with different group velocities and the phase relationship between spatial locations become decorrelated over distance, leading to a loss of spatial coherence. The distance over which this spatial decoherence

Optics EXPRESS

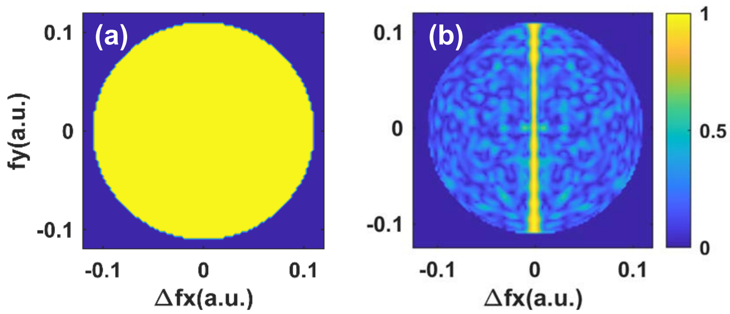

Fig. 7. Simulated spatial coherence in the cases of (a) monochromatic excitation and (b) broadband excitation. Δfx and fy represent the spatial frequencies in Fourier domain corresponding to Δx and y.

occurs depends on the number of excited modes and the ratio of modal dispersion to the coherence time of the source $\Delta\tau_m/\tau_c$, where $\Delta\tau_m$ and τ_c denote the modal dispersion and coherence time, respectively [26]. The coherence time is inversely related to the source bandwidth, while the modal dispersion can be approximated as $L(\mathrm{NA})^2/2nc$, where L is the fiber length, NA is the numerical aperture, n is the refractive index, and c is the speed of light. When $\Delta\tau_m/\tau_c >>1$, the differential delays between the modes exceed the temporal coherence of the source, and the output field becomes spatially incoherent. In our experiment, the source has a bandwidth of 45 nm, corresponding to a coherence time of approximately 178 fs. The modal dispersion in the fiber is estimated to be around 0.61 ns, which is orders of magnitude larger than the coherence time, resulting in an output field essentially spatially incoherent. In the case of a quasi-monochromatic source however, the coherence time is much longer than the modal dispersion and the spatial coherence is preserved.

4. Quantitative coherence control with a MMF

The results above highlighted the central role of the light source bandwidth in determining the spatial coherence at the MMF output. This suggests that one may design a light source that combines a specific number of narrow-band sources with different central wavelengths, similar to a spectrally incoherent optical frequency comb, whose spatial control can be effectively controlled by propagation in a MMF. In a practical implementation, two important parameters come into play: the number of individual spectral components that are combined and the minimum wavelength-spacing Δλ between two spectral components. In what follows, we quantify the impact of these two parameters, both theoretically and experimentally, and a simple model is proposed for manipulating the coherence of such a light source.

In order to simulate the spatial coherence $\gamma(\Delta\lambda,N_\lambda)$, we use the same approach as in the previous section. Figure 8(a) shows the simulated average degree of spatial coherence as a function of the number of combined spectral components and for different wavelength-spacing values of 0.05 nm, 0.1 nm, 0.2 nm, and 1 nm. Similarly to the average degree of spectral coherence employed to characterize the spectral coherence of supercontinuum light [25], we introduce an averaged degree of spatial coherence $g_A^{(\Delta\lambda,N_\lambda)}$ to quantify the overall spatial coherence of the beam:

$$g_A^{(\Delta\lambda,N_\lambda)} = \frac{\iint \gamma^{(\Delta\lambda,N_\lambda)}(\Delta x, y)\cdot I_b(\Delta x, y)dxdy}{\iint I_b(\Delta x, y)dxdy}, \tag{12}$$

where $\Delta\lambda$ represents the wavelength-spacing between two spectral components and N_λ denotes the total number of discrete combined spectral components. $\gamma(\Delta\lambda,N_\lambda)$ represents the calculated

Optics EXPRESS

2D spatial coherence distribution across the transverse plane of the beam and I_b corresponds to the spatial intensity profile of the beam. The parameter ${g_A}^{(\Delta\lambda,N\lambda)}$ is a positive number in the range 0 to 1 corresponding to fully spatially incoherent and coherent beams, respectively. One can see that the average spatial coherence generally decreases with the number of spectral components, and that it decreases more rapidly for a larger wavelength-spacing. This can be understood from the fact that smaller wavelength spacing corresponds to minor discrepancies in propagation constants for the same mode in the fiber, resulting in reduced local phase differences among all modes and requiring more spectral components to achieve significant coherence reduction. We next validated these simulations experimentally by emulating a light source composed of multiple spectral components whose wavelength-spacing can be tuned. For this purpose, we use the tunable quasi-monochromatic laser with 10 kHz linewidth where the wavelength can be varied in steps of 1 pm over the 1500-1600 nm range connected to the MMF and we acquire interferograms while scanning the path difference between the two WFI arms. These interferograms are then overlaid in post-data processing to obtain the maximum and minimum spatial intensity at each camera pixel, from which the visibility and spatial coherence are calculated. An example of emulated multi-wavelengths light source characteristics with 25 discrete spectral components evenly spaced by 0.2 nm is shown in Fig. 9. The averaged spatial coherence for different wavelength-spacing and number of spectral components is shown in Fig. 8(b). The emulated experimental results are in good agreement with the simulation results, in particular the average spatial coherence decreases with the number of spectral components and decoherence increases for a wider wavelength-spacing. We note that in the experiments the coherence is generally lower than in the simulations, which can be attributed to the camera resolution limit and noise.

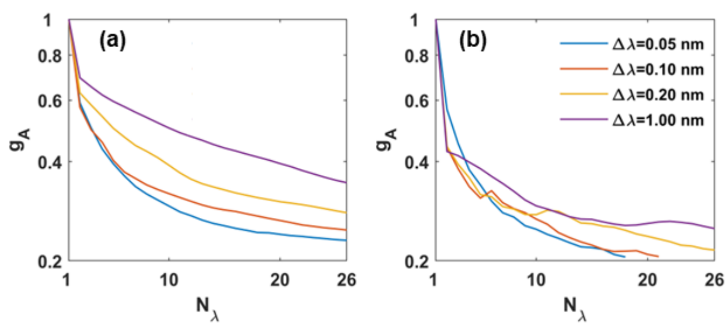

Fig. 8. Averaged degree of spatial coherence of a spectrally incoherent comb-like source vs with number for discrete spectral components and spacing: (a) numerical simulation and (b) experiments.

5. Conclusion

Understanding the underlying physics of coherence control in MMFs is important for practical applications and further developments. While speckle contrast has been widely used as an indicator of spatial coherence, it does not always accurately reflect coherence levels. Advanced methods, such as spatial interferometry and wavefront-folding interferometers have proven more effective for characterizing coherence, overcoming practical challenges to provide high efficiency and flexibility in measuring arbitrary fields. Using a wavefront-folding interferometer, we have characterized the coherence degree at the output of a MMF across the full beam and showed how spatial coherence is significantly reduced with energy redistribution towards higher-order modes. Modal expansion and random mode coupling theory were applied to calculate mode amplitudes, with simulated coherence degree showing excellent agreement with experimental findings. The coherence reduction is attributed to the scrambling of phase distribution from different spectral

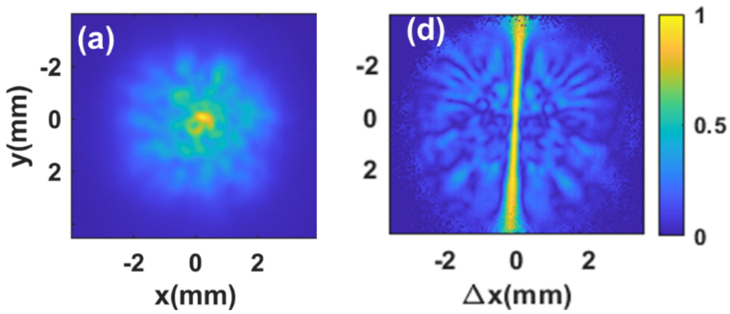

Fig. 9. Experimental validation of tunable coherence in a MMF using a discrete set of quasi-monochromatic lasers. (a) Intensity from overlapping speckle patterns of different wavelengths. (b) is the computed spatial coherence.

components within the MMF. This was further demonstrated through interferograms of multiple quasi-monochromatic sources. Our work provides valuable insights for improving coherence management for practical fiber-optic applications in spatial imaging and sensing.

Funding. Research Council of Finland (320165, 346511, 368650); China Scholarship Council; Väisälän Rahasto.

Acknowledgments. We acknowledge the support of the Academy of Finland (320165, 346511, 368650), China Scholarship Council, and Vilho, Yrjö ja Kalle Väisälän Rahasto.

Disclosures. The authors declare no competing financial interests.

Data availability. The data that support the findings of this work are available from the corresponding author upon reasonable request.

References

1. D. A. Boas and A. K. Dunn, "Laser speckle contrast imaging in biomedical optics," J. Biomed. Opt. **15**(1), 011109 (2010).
2. R. Ma, W. L. Zhang, J. Y. Guo, *et al.*, "Decoherence of fiber supercontinuum light source for speckle-free imaging," Opt. Express **26**(20), 26758–26765 (2018).
3. Y. Garini, I. T. Young, and G. McNamara, "Spectral imaging: principles and applications," Cytometry, Part A **69A**, 735–747 (2006).
4. S. M. Kolenderska, O. Katz, M. Fink, *et al.*, "Scanning-free imaging through a single fiber by random spatio-spectral encoding," Opt. Lett. **40**(4), 534–537 (2015).
5. A. Efimov, K. Velizhanin, and G. Gelikonov, "Simultaneous scintillation measurements of coherent and partially coherent beams in an open atmosphere experiment," Proc. SPIE **8971**, 897105 (2014).
6. T. Stangner, H. Zhang, T. Dahlberg, *et al.*, "Step-by-step guide to reduce spatial coherence of laser light using a rotating ground glass diffuser," Appl. Opt. **56**(19), 5427–5435 (2017).
7. K. Goda, K. K. Tsia, and B. Jalali, "Serial time-encoded amplified imaging for real-time observation of fast dynamic phenomena," Nature **458**(7242), 1145–1149 (2009).
8. R. Ma, J. Q. Li, J. Y. Guo, *et al.*, "High-power low spatial coherence random fiber laser," Opt. Express **27**(6), 8738–8744 (2019).
9. D. S. Mehta, D. N. Naik, R. K. Singh, *et al.*, "Laser speckle reduction by multimode optical fiber bundle with combined temporal, spatial, and angular diversity," Appl. Opt. **51**(12), 1894–1904 (2012).
10. C. Pask and A. W. Snyder, "The Van-Citter Zernike theorem for optical fibers," Opt. Commun. **9**(1), 95–97 (1973).
11. B. Crosignani and P. Di Porto, "Coherence of an electromagnetic field propagating in a weakly guiding fiber," J. Appl. Phys. **44**(10), 4616–4617 (1973).
12. B. Crosignani, B. Diano, and P. Di Porto, "Interference of mode patterns in optical fibers," Opt. Commun. **11**(2), 178–179 (1974).
13. E. Hernandez, M. M. Roth, K. Petermann, *et al.*, "Mode expansion theory and application in step-index multimode fibers for astronomical spectroscopy," J. Opt. Soc. Am. B **38**(7), A36–A50 (2021).
14. A. Efimov, "Spatial coherence at the output of multimode optical fibers," Opt. Express **22**(13), 15577–15588 (2014).
15. M. I. Dzhibladze, B. S. Lezhava, and T. Y. A. Chelidze, "Coherence of laser radiation traveling along an optical fiber," Sov. J. Quantum Electron. **4**(10), 1181–1183 (1975).
16. P. Spano, "Connection between spatial coherence and modal structure in optical fibers and semiconductor lasers," Opt. Commun. **33**(3), 265–270 (1980).

Optics EXPRESS

17. C. Iaconis and I. A. Walmsley, "Direct measurement of the two-point field correlation function," Opt. Lett. **21**(21), 1783–1785 (1996).
18. M. Born and E. Wolf, *Principles of Optics* (Cambridge University Press, 1999).
19. M. Koivurova, H. Partanen, J. Lahyani, *et al.*, "Scanning wavefront folding interferometers," Opt. Express **27**(5), 7738–7750 (2019).
20. A. Halder, H. Partanen, A. Leinonen, *et al.*, "Mirror-based scanning wavefront-folding interferometer for coherence measurements," Opt. Lett. **45**(15), 4260–4263 (2020).
21. J. Turunen, A. Halder, M. Koivurova, *et al.*, "Measurement of spatial coherence of light [Invited]," J. Opt. Soc. Am. A **39**(12), C214–C239 (2022).
22. K. Okamoto, *Fundamentals of Optical Waveguides* (Elsevier, 2021).
23. T. Kaiser, D. Flamm, S. Schröter, *et al.*, "Complete modal decomposition for optical fibers using CGH-based correlation filters," Opt. Express **17**(11), 9347–9356 (2009).
24. D. Gloge, "Optical power flow in multimode fibers," Bell Syst. Tech. J. **51**(8), 1767–1783 (1972).
25. J. M. Dudley, G. Genty, and S. Coen, "Supercontinuum generation in photonic crystal fiber," Rev. Mod. Phys. **78**(4), 1135–1184 (2006).
26. A. Efimov, "Coherence and speckle contrast at the output of a stationary multimode optical fiber," Opt. Lett. **43**, 4767–4770 (2018).